

A ONE-POINT INTEGRATION QUADRILATERAL WITH HOURLASS CONTROL IN AXISYMMETRIC GEOMETRY

P. MATEJOVIČ and V. ADAMÍK

Nuclear Power Plants Research Institute, 918 64 Trnava, Czechoslovakia

Received 15 July 1987

Revised manuscript received 29 February 1988

A one-point integration scheme which analytically integrates element volume and uniform strain modes for general isoparametric quadrilateral in axisymmetric geometry is described. A method for isolating proper hourglass modes is presented. It is shown that these modes rather differ from hourglass modes in plane Cartesian geometry, especially near the axis of symmetry. A simple elastic and viscous hourglass control scheme is presented and discussed. Bounds on the quadrilateral eigenvalues that provide stable time steps for explicit time integration algorithms are obtained considering isotropic hypoelastic material. Numerical examples demonstrate the effectiveness of the developed technique for finite element code.

1. Introduction

Many problems in structural analyses are axisymmetric and can be reduced to two-dimensional problems. One-point integration substantially reduces the number of evaluations of the semidiscretized gradient operator, commonly known as the B matrix, and the constitutive equations. The latter effect is significant mainly in nonlinear problems. At the same time, the rate of convergence of the one-point integration elements is comparable to that of the fully integrated elements.

The major drawback of one-point integration elements is a mesh instability known as hourglassing or keystoneing. A very effective hourglass control has been developed for two- and three-dimensional Cartesian geometry [1, 2, 8]. However, as regards axisymmetric geometry, the hourglass control is usually approximated [5] using the modified plane hourglass control scheme which does not meet the patch test.

In this paper, we follow ideas of Belytschko and his coworkers [1–3].

Firstly, a technique which analytically integrates the element volume and the uniform strain modes for general quadrilateral element in axisymmetric geometry is described.

It is shown, that the null space or kernel of the discrete gradient operator B consists of four vectors. Two of those correspond to rigid-body motion and two other are hourglass modes in the r - and z -direction. They differ from hourglass modes in plane geometry, especially for the elements near the axis of symmetry. However, for elements quite far from the axis, they converge to the plane hourglass modes.

To control these hourglass modes we introduce two additional generalized strains which combined with \mathbf{B} increase the rank of \mathbf{B} from four to six.

To provide stable time steps for explicit time integration algorithm, we evaluate the bounds on the quadrilateral element eigenvalues supposing isotropic hypoelastic material. It is shown that, due to azimuthal stresses, the elements near the axis are stiffer than the ones far from axis.

Two numerical examples computed by FINEDAN code [4] with boundary conditions that make possible hourglass modes occurrence are presented and discussed.

Without hourglass control, the solutions quickly degenerate. The plane hourglass control applied to axisymmetric problems and the newly developed technique are compared.

2. Basic relations

If domain, forces, and constraints are axisymmetric, it is convenient to formulate the problem in the cylindrical coordinate system r, φ, z . The displacement vector, strain, and stress tensors $\mathbf{u}, \boldsymbol{\varepsilon}, \boldsymbol{\sigma}$ do not depend on azimuthal coordinate φ and thus one obtains a two-dimensional formulation in the r - z plane.

In curvilinear coordinates, the strain tensor is defined differently from that in Cartesian coordinates. The difference between the two is an additional term containing the Cristoffel symbols, which have in the cylindrical coordinate system an especially simple form [6]. The strain tensor is, supposing small strain theory, given by

$$\begin{aligned} \varepsilon_{rr} &= \frac{\partial u_r}{\partial r}, & \varepsilon_{\varphi\varphi} &= \frac{u_r}{r}, & \varepsilon_{zz} &= \frac{\partial u_z}{\partial z}, \\ \varepsilon_{r\varphi} &= 0, & \varepsilon_{rz} &= \frac{1}{2} \left(\frac{\partial u_z}{\partial r} + \frac{\partial u_r}{\partial z} \right), & \varepsilon_{\varphi z} &= 0. \end{aligned} \quad (1)$$

The principles of virtual power and boundary conditions are

$$\begin{aligned} & \int_A \rho(\ddot{u}_r \delta \dot{u}_r + \ddot{u}_z \delta \dot{u}_z) r \, dA = \\ & - \int_A (\sigma_{rr} \delta \dot{\varepsilon}_{rr} + \sigma_{zz} \delta \dot{\varepsilon}_{zz} + \sigma_{\varphi\varphi} \delta \dot{\varepsilon}_{\varphi\varphi} + 2\sigma_{rz} \delta \dot{\varepsilon}_{rz}) r \, dA \\ & + \int_A (b_r \delta \dot{u}_r + b_z \delta \dot{u}_z) r \, dA + \int_{S_I} (T_r \delta \dot{u}_r + T_z \delta \dot{u}_z) r \, dS, \end{aligned} \quad (2)$$

$$\begin{aligned} \mathbf{T} &= \mathbf{T}^* \quad \text{on } S_T, & S_T \cap S_u &= \emptyset, \\ \mathbf{u} &= \mathbf{u}^* \quad \text{on } S_u, \end{aligned} \quad (3)$$

where superposed dots designate time derivatives, $*$ denotes variables prescribed on the boundary, δ denotes variation of the subsequent variable, ρ is density, b_i is the external body

force in the i th direction ($i = r, z$), T_i denotes the external surface forces, A is the domain area in the r - z plane, S_T is a part of boundary loaded by surface forces, and S_u is a part of boundary with a given displacement.

We discretize the area A into a number of the isoparametric quadrilateral elements. Standard indicial notation will be used: lower-case subscripts denote the components of tensor or vector, upper-case subscripts denote nodes, and repeated subscripts imply a summation over the range of the index. A comma followed by a subscript designates a partial derivative with respect to the following spatial variable.

The quadrilateral element coordinates x_i ($x_1 = r$; $x_2 = z$) are expressed by

$$x_i = x_{iI} \Phi_I(\xi, \eta), \quad (4)$$

where Φ_I are isoparametric shape functions.

The same shape functions are used for the element displacement and velocity field:

$$u_i = u_{iI} \Phi_I, \quad \dot{u}_i = \dot{u}_{iI} \Phi_I. \quad (5)$$

The shape functions can be conveniently expanded in terms of an orthogonal set of base vectors:

$$\Phi(\xi, \eta) = \frac{1}{4} s + \frac{1}{2} \xi \Lambda_1 + \frac{1}{2} \eta \Lambda_2 + \xi \eta h, \quad (6)$$

where

$$\begin{aligned} s^t &= [1, 1, 1, 1], & h^t &= [1, -1, 1, -1] \\ \Lambda_1^t &= [-1, 1, 1, -1], & \Lambda_2^t &= [-1, -1, 1, 1]. \end{aligned} \quad (7)$$

The following additional column vectors will be useful:

$$r^t = [r_1, r_2, r_3, r_4], \quad z^t = [z_1, z_2, z_3, z_4], \quad (8)$$

where numbers denote element nodes.

Following the finite element technique and using the lumped mass approach, the semidiscrete equation corresponding to (2) is

$$M \ddot{u}_i = -f_i^{\text{int}} + f_i^{\text{ext}}, \quad (9)$$

where M is the mass matrix, and f_i^{int} and f_i^{ext} are internal and external nodal force vectors.

The lumped mass approach has been chosen in the following form:

$$M_{IJ} = 0, \quad I \neq J, \quad M_{II} = \int_A \rho \Phi_I r \, dA \quad (\text{no sum on } J), \quad (10)$$

where A is the element area in the r - z plane.

This form of the mass matrix elements allocates more mass to the nodes with greater radius,

while the often used “ $\frac{1}{4}$ approach” divides element mass equally among each node. The difference is especially important on and near the axis. Furthermore, (10) respects the true distribution of element mass for a nonrectangular element both in cylindrical and Cartesian plane geometries. The main shortcoming of this approach is the necessity to recalculate node mass according to the element deformation.

REMARK 2.1. For problems with low element deformation the node mass can be considered constant and has to be computed only at the start of the analysis.

REMARK 2.2. The integral in (10) is evaluated analytically. It involves integration of a polynomial by the same method as presented in Appendix A.

The evaluation of the external force vectors f_i^{ext} does not represent any problem and can be obtained by a standard procedure.

We concentrate on the internal force vectors f_i^{int} and perform one-point integration considering a state of uniform stress and strain. Then the internal forces are

$$\begin{aligned} f_r^{\text{int}} &= \sigma_{rr} b_r + \sigma_{rz} b_z + \sigma_{\varphi\varphi} c, \\ f_z^{\text{int}} &= \sigma_{rz} b_r + \sigma_{zz} b_z, \end{aligned} \quad (11)$$

where σ_{ij} represents uniform stress field and vectors b_i and c are given by

$$b_i = \int_A \Phi_i r \, dA, \quad c = \int_A \Phi \, dA. \quad (12)$$

As follows from Appendix A, both integrals in (12) lead to a similar type of numerical expression.

The vectors are obtained as a linear combination of base vectors:

$$b_i = b_i(\Lambda_1, \Lambda_2, h), \quad c = c(s, \Lambda_1, \Lambda_2). \quad (13)$$

REMARK 2.3. Note the difference between cylindrical and Cartesian plane geometries. In the latter case b_i is a linear combination of Λ_1, Λ_2 vectors only.

The following useful relations can be verified from Appendix A and (7):

$$\begin{aligned} b_i^t x_j &= V \delta_{ij}, & c^t h &= 0, & c^t r &= V, \\ b_i^t s &= 0, & c^t s &= A, & s^t h &= 0. \end{aligned} \quad (14)$$

3. Hourglass modes

The deformation of the material is characterized by the strain rate tensor

$$\dot{\epsilon}^t = [\dot{\epsilon}_r, \dot{\epsilon}_z, \dot{\epsilon}_\varphi, 2\dot{\epsilon}_{rz}]. \quad (15)$$

The discrete operator \mathbf{B} for a cylindrical quadrilateral with one-point quadrature is given by

$$\mathbf{B} = \begin{bmatrix} \mathbf{b}_r^t & \mathbf{0}^t \\ \mathbf{0}^t & \mathbf{b}_z^t \\ \mathbf{c}^t & \mathbf{0}^t \\ \mathbf{b}_z^t & \mathbf{b}_r^t \end{bmatrix}, \quad (16)$$

where $\mathbf{0}$ is a null vector.

Thus it holds:

$$\dot{\boldsymbol{\varepsilon}} = \frac{1}{V} \mathbf{B} \dot{\mathbf{d}}, \quad (17)$$

where

$$\mathbf{d} = \begin{Bmatrix} u_r \\ u_z \end{Bmatrix}, \quad (18)$$

and V is the element volume.

The matrix \mathbf{B} is of rank 4. From it results that the null-space or kernel of the operator \mathbf{B} consists of four linearly independent vectors:

$$\mathbf{d}_i = [\mathbf{d}_1, \mathbf{d}_2, \mathbf{d}_3, \mathbf{d}_4]. \quad (19)$$

To find the null-space of \mathbf{B} it is necessary to solve

$$\mathbf{B} \mathbf{d} = \mathbf{0}. \quad (20)$$

For this purpose it is convenient to expand each component of the unknown vector \mathbf{d} as a linear combination of vectors \mathbf{s} , \mathbf{r} , \mathbf{z} , and \mathbf{h} . These vectors are for any nondegenerate quadrilateral linearly independent and span the four-dimensional space \mathbb{R}^4 . Using the relations (14) we obtain four vectors of (19) which span the null-space of \mathbf{B} . From these vectors it is necessary to distinguish the rigid-body motion and hourglass deformations.

The first vector \mathbf{d}_1 is easy to find. It corresponds to an arbitrary rigid-body translation in the z -direction, see Fig. 1,

$$\mathbf{d}_1 = \begin{Bmatrix} \mathbf{0} \\ s \end{Bmatrix}. \quad (21)$$

The second vector \mathbf{d}_2 is a combination of a rigid-body rotation and a unique translation in the r -direction, see Fig. 1,

$$\mathbf{d}_2 = \begin{Bmatrix} \frac{1}{A} (\mathbf{c}^t \mathbf{z}) \mathbf{s} - \mathbf{z} \\ \mathbf{r} \end{Bmatrix}. \quad (22)$$

The two-dimensional space spanned by \mathbf{d}_1 and \mathbf{d}_2 will be called the proper null-space of \mathbf{B} .

The third and fourth vectors are spurious singular or hourglass modes associated with displacement fields, for which the strains should not vanish. They have been chosen in the

following form:

$$d_3 = \begin{Bmatrix} \gamma \\ 0 \end{Bmatrix}, \quad (22a)$$

$$d_4 = \begin{Bmatrix} 0 \\ \gamma \end{Bmatrix}, \quad (22b)$$

where

$$\gamma = \frac{1}{VA} [(c^t x_i)(b_i^t h)] s - \frac{1}{V} (b_i^t h) x_i + h. \quad (22c)$$

The two-dimensional space spanned by d_3 and d_4 will be called the improper null-space of B matrix.

In Figs 2–4 there is shown difference between hourglass modes in plane Cartesian geometry, given by vector h , and hourglass modes in cylindrical plane geometry, given by vector γ .

REMARK 3.1. From Figs 2–4 we can see:

- The difference between cylindrical γ and Cartesian h vectors is significant only near the axis.
- HG modes in the r -direction can occur near the axis mainly for problems with a central axial cavity.
- From the compatibility equation it follows that if HG modes in z -direction propagate to the axis, they will be amplified.

4. Hourglass control

To control HG modes, we introduce two additional generalized strains, q_i , which, when combined with B , span the complement of the proper null-space and we obtain the B^* matrix that is of rank 6. The resulting matrix and formula for generalized strains are

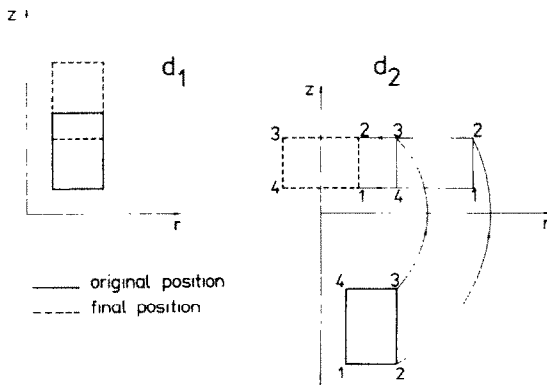


Fig. 1. Proper null-space vectors d_1 and d_2 .

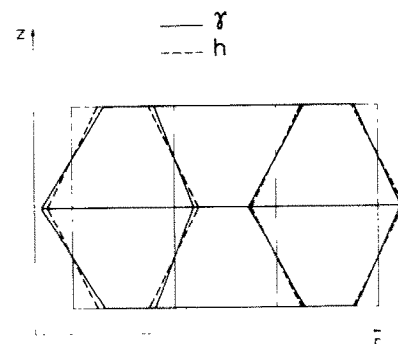


Fig. 2. Difference between h and γ modes in the r -direction (improper null-space vector d_3).

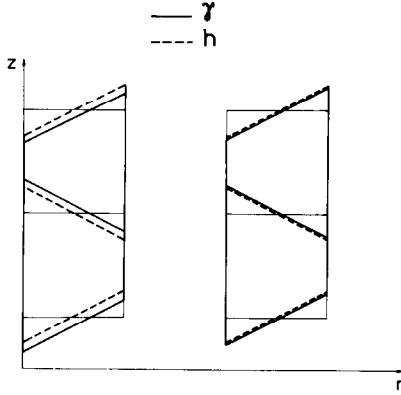


Fig. 3. Difference between h and γ modes in the z -direction (improper null-space vector d_4).

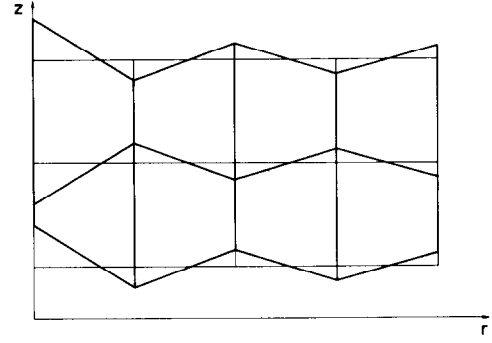


Fig. 4. Cylindrical HG modes in the z -direction with compatibility condition.

$$B^* = \begin{bmatrix} b_r^t & 0^t \\ 0^t & b_z^t \\ c^t & 0^t \\ b_z^t & b_r^t \\ \gamma^{*t} & 0^t \\ 0^t & \gamma^{*t} \end{bmatrix}, \quad (23)$$

$$\dot{q}_i = \frac{1}{V} \gamma^{*t} \dot{u}_i. \quad (24)$$

The discrete operator B performs properly on *linear fields* which means

$$u_i = k_1 s + k_2 r + k_3 z, \quad (25)$$

where k_1 , k_2 , and k_3 are arbitrary constants.

To maintain this desirable property, the cylindrical shape vector γ^* should not have any effect on linear fields. Therefore, γ^* has been chosen as follows:

- For any nodal values associated with linear fields $q_i = 0$, it means that γ^* is orthogonal to linear fields.
- If u_i is in the improper null-space, $q_i \neq 0$.

It is convenient to choose the new base of \mathbb{R}^4 by means of b_r , b_z , c , γ vectors. To obtain γ^* , we expand it in terms of these base vectors:

$$\gamma^* = a_1 b_r + a_2 b_z + a_3 c + a_4 \gamma. \quad (26)$$

Substituting (26) and (25) into (24) and using (14) we obtain

$$k_1(a_3 A + a_4 \gamma^t s) + k_2(a_1 V + a_3 c^t r + a_4 \gamma^t r) + k_3(a_2 V + a_3 c^t z + a_4 \gamma^t z) = 0. \quad (27)$$

Since the above expression must be valid for arbitrary k_i , it follows that

$$\begin{aligned} a_3 &= -a_4/A\boldsymbol{\gamma}^t\mathbf{s}, \\ a_i &= a_4/V\left[\frac{\boldsymbol{\gamma}^t\mathbf{s}}{A}(\mathbf{c}^t\mathbf{x}_i) - (\boldsymbol{\gamma}^t\mathbf{x}_i)\right], \quad i = 1, 2, \end{aligned} \quad (28)$$

where a_4 is an arbitrary constant.

To ensure the formal consistency of (17) and (24) we have chosen $a_4 = V$.

Therefore, the final form of the cylindrical shape vector is

$$\boldsymbol{\gamma}^* = V\boldsymbol{\gamma} - \frac{V}{A}(\boldsymbol{\gamma}^t\mathbf{s})\mathbf{c} + \left[\frac{1}{A}(\boldsymbol{\gamma}^t\mathbf{s})(\mathbf{c}^t\mathbf{x}_i) - \boldsymbol{\gamma}^t\mathbf{x}_i\right]\mathbf{b}_i. \quad (29)$$

REMARK 4.1. The differences between the cylindrical HG mode vector $\boldsymbol{\gamma}$ and shape vector $\boldsymbol{\gamma}^*$ are the following:

- $\boldsymbol{\gamma}$ is orthogonal to $\mathbf{b}_r, \mathbf{b}_z, \mathbf{c}$;
- $\boldsymbol{\gamma}^*$ is orthogonal to an arbitrary linear field;
- $\boldsymbol{\gamma}^{*t}\boldsymbol{\gamma} = V\boldsymbol{\gamma}^t\boldsymbol{\gamma}$.

Let $\boldsymbol{\sigma}$ denote the Cauchy stress tensor arranged in a column matrix:

$$\boldsymbol{\sigma}^t = [\sigma_{rr}, \sigma_{zz}, \sigma_{\varphi\varphi}, \sigma_{rz}], \quad (30)$$

and let \mathbf{Q} be the generalized HG stress tensor, corresponding to the generalized strains \mathbf{q} .

Then the internal nodal forces are

$$\mathbf{f}^{\text{int}} = \begin{Bmatrix} \mathbf{f}_r^{\text{int}} \\ \mathbf{f}_z^{\text{int}} \end{Bmatrix} = \mathbf{B}^{*t} \begin{Bmatrix} \boldsymbol{\sigma} \\ \mathbf{Q} \end{Bmatrix} = \mathbf{B}^t \boldsymbol{\sigma} + \begin{bmatrix} \boldsymbol{\gamma}^* & \mathbf{0} \\ \mathbf{0} & \boldsymbol{\gamma}^* \end{bmatrix} \mathbf{Q}. \quad (31)$$

For anisotropic hypoelastic material, the stress-strain relation is given by Hooke's law:

$$\begin{Bmatrix} \sigma_r^\nabla \\ \sigma_z^\nabla \\ \sigma_\varphi^\nabla \\ \sigma_{rz}^\nabla \end{Bmatrix} = \begin{bmatrix} \lambda + 2\mu & \lambda & \lambda & 0 \\ \lambda & \lambda + 2\mu & \lambda & 0 \\ \lambda & \lambda & \lambda + 2\mu & 0 \\ 0 & 0 & 0 & \mu \end{bmatrix} \begin{Bmatrix} \dot{\epsilon}_r \\ \dot{\epsilon}_z \\ \dot{\epsilon}_\varphi \\ 2\dot{\epsilon}_{rz} \end{Bmatrix}, \quad (32)$$

where the symbol ∇ denotes a frame-invariant rate and Lamé coefficients need not be constant.

The physical stress rate for such a material is given by

$$\begin{aligned} \dot{\sigma}_{ij} &= \sigma_{ij}^\nabla + W_{ik}\sigma_{kj} + W_{jk}\sigma_{ki}, \quad i, j, k = 1, 2, \\ \dot{\sigma}_{\varphi\varphi} &= \sigma_{\varphi\varphi}^\nabla, \end{aligned} \quad (33)$$

where

$$W_{ij} = \frac{1}{2}(\dot{u}_{i,j} - \dot{u}_{j,i}). \quad (34)$$

Two methods for alleviating hourglass difficulties are presented here:

- (1) application of artificial stiffness to the HG modes (elastic HG control);
- (2) application of artificial damping to the HG modes (viscous HG control).

The intent of the second approach is to allow some hourglassing, but prevent violent oscillations. A shortcoming of this approach is that, since there is no stiffness in the HG modes, mesh distortion in these modes is permanent. Furthermore, the explicit time step stability limit is lowered substantially by damping [2] and application of this approach leads to a loss of energy of considered system.

The elastic HG control conserves the energy and cannot decrease the stability limit (at least for small values of κ).

The constitutive laws for the generalized HG stresses and strains are supposed to have simple forms:

$$Q_i^\nabla = \frac{1}{V} \kappa K_{\max} \dot{q}_i, \quad \dot{Q}_i = Q_i^\nabla + W_{ik} Q_k, \quad (35a)$$

for artificial stiffness, and

$$Q_i = 2\varepsilon\omega_{\max}(\tfrac{1}{4}\rho)\dot{q}_i \quad (35b)$$

for artificial damping. K_{\max} and ω_{\max} in (35) are the maximum stiffness and maximum frequency of the element and κ and ε are the stiffness and damping coefficients.

As follows from Appendix B, the maximum stiffness and frequency for cylindrical quadrilateral are bounded by

$$\frac{1}{3V} (\lambda + 2\mu)(\mathbf{b}_i^t \mathbf{b}_i + \mathbf{c}^t \mathbf{c}) \leq K_{\max} \leq \frac{1}{V} (\lambda + 2\mu)(\mathbf{b}_i^t \mathbf{b}_i + \mathbf{c}^t \mathbf{c}), \quad (36a)$$

$$\sqrt[4]{\frac{\lambda + 2\mu}{\rho} \frac{\mathbf{b}_i^t \mathbf{b}_i + \mathbf{c}^t \mathbf{c}}{V^2}} \leq \omega_{\max} \leq 2\sqrt{\frac{\lambda + 2\mu}{\rho} \frac{\mathbf{b}_i^t \mathbf{b}_i + \mathbf{c}^t \mathbf{c}}{V^2}}. \quad (36b)$$

The threshold of the effective HG stabilization for both types of HG control must be determined empirically through the values of HG control parameters κ and ε .

REMARK 4.2 More general constitutive laws than those given by (35) can be found by using the Hu–Washizu variational principle [1, 7].

REMARK 4.3. As follows from (36a), the elements near the axis are relatively stiffer than those far from the axis due to the term

$$\frac{\mathbf{c}^t \mathbf{c}}{V} \doteq \frac{1}{4} \frac{A^2}{V},$$

which converges to zero as the element moves away from the axis.

REMARK 4.4. The evaluation of the element maximum frequency is also necessary to provide a stable time step for explicit time integration algorithm.

REMARK 4.5. Upper bounds given by (36) are used for the maximum frequency and stiffness in (35).

5. Results and discussion

Two numerical examples are reported to demonstrate HG modes and their control in cylindrical axisymmetric geometry.

The purpose of these examples is:

- to show that in general, HG control is necessary to obtain a reasonable solution with one-point integration elements;
- to show that cylindrical HG modes differ from those in Cartesian plane geometry, as described in Section 3;
- to demonstrate the effectiveness of the developed integration scheme and HG control;
- to compare elastic and viscous HG control;
- to compare developed integration scheme and HG control with those based on plane approach;
- to estimate and compare rate of convergence for both above-mentioned approaches.

For all presented computations, the term γ^*/V in (24) and (31) was normalized for unity and an explicit time integration scheme was used. The mass matrix was computed only at start of the analysis. All presented results were obtained by using the FINEDAN code [4].

EXAMPLE 5.1 A cylindrical plate, simply supported on the outer radius, with the mesh shown in Fig. 5 was considered. The linear Hooke's law was used with the following material parameters: $\rho = 1000 \text{ kg} \cdot \text{m}^{-3}$, $\lambda = 0$, $\mu = 5 \cdot 10^8 \text{ Pa}$. A uniform pressure $p = 15 \times 10^5 \text{ Pa}$ was applied as a step function on the upper plate surface. It excited the first mode of the plate.

This problem illustrates the HG modes, especially in the z -direction.

Figure 6 shows the solution without any HG control. It confirms our earlier theoretical conclusions described in Remark 3.1. It is evident that the solution rapidly becomes meaningless. Figures 7–9 show the displacement time history of point A and mesh distortions

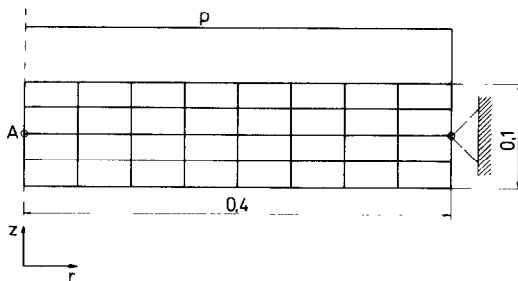


Fig. 5. Example 5.1, cylindrical plate, simply supported on outer radius. Problem definition.

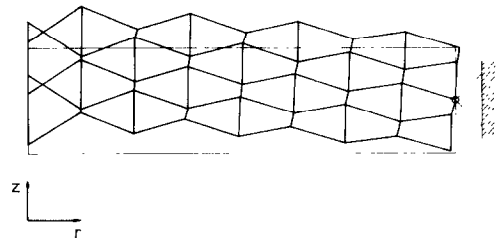


Fig. 6. Mesh deformation with no HG control at time 1.8 ms.

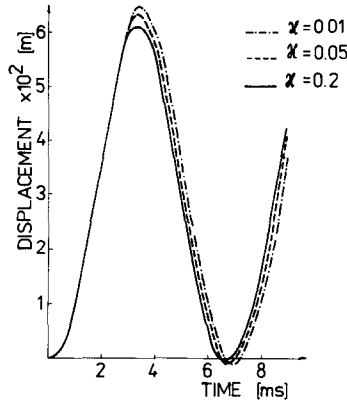


Fig. 7. Displacement of point A for various values of parameter κ .

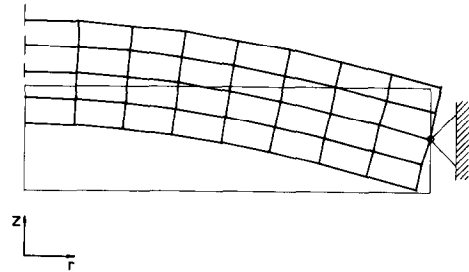


Fig. 8. Mesh deformation at time 3.69 ms for $\kappa = 0.01$.

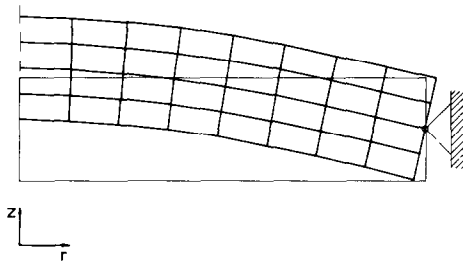


Fig. 9. Mesh deformation at time 3.64 ms for $\kappa = 0.2$.

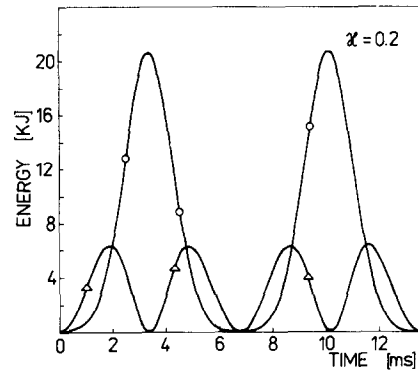


Fig. 10. Total kinetic and deformation energy for $\kappa = 0.2$. O : deformation energy; Δ : kinetic energy.

for various elastic HG control parameters κ . We can see, that even a small $\kappa = 0.01$ stabilizes the mesh quite well.

Figures 10 and 11 illustrate the time history of total kinetic, deformation and HG energy of the plate for $\kappa = 0.2$. These histories confirm the conservation of total energy by using an elastic HG control. A gradual increase of the HG energy and partial asymmetry of its peaks in Fig. 11 are caused by an error accumulation due to an inherent asynchronization in computation of the HG energy.

Figures 12–14 show the displacement time history of point A and mesh distortion for various viscous HG control parameters ε . Although the HG viscosity slows down the HG distortion, we can see that even the value $\varepsilon = 0.2$ does not stabilize the mesh completely and a reasonable solution in displacement is obtained only through one period.

Figure 15 illustrates the time history of total kinetic, deformation and dissipated HG energy of the plate for $\varepsilon = 0.2$. From this figure and from Fig. 12 it follows that reasonable solution through more than one period can be obtained only by using the values of ε greater than 0.2.

The fact that the dissipative energy decreases with increasing of the HG viscous parameter ε seems to be paradoxical but we do remember that the viscous HG damping acts only on the

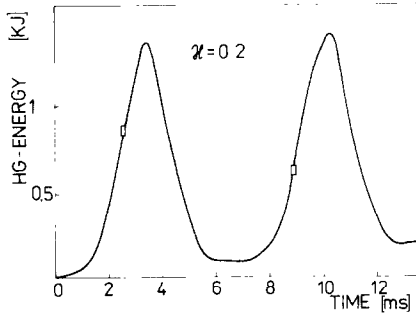
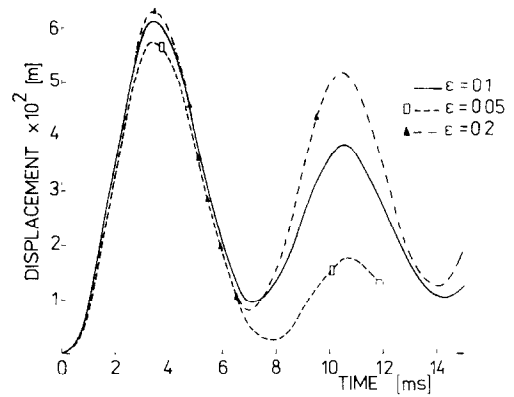
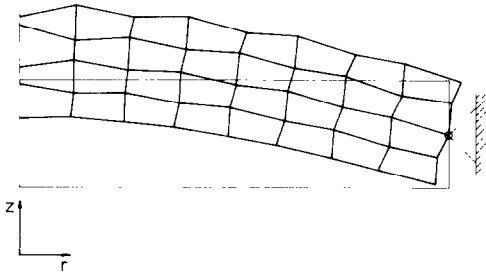
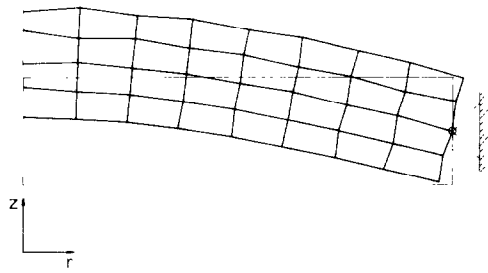


Fig. 11. Elastic HG energy time history.

Fig. 12. Displacement of point A for various values of parameter ϵ . Symbol \circ denotes negative area for upper element on the axis of symmetry.Fig. 13. Mesh deformation at time 3.45 ms for $\epsilon = 0.1$.Fig. 14. Mesh deformation at time 3.21 ms for $\epsilon = 0.2$.

HG part of the velocity field. Furthermore, a high value of ϵ substantially reduces the stable time step. Therefore, the elastic HG control seems to be more suitable as the viscous one.

Example 5.1 was also computed with the mass matrix given by (10), but in this case the matrix was determined at each time step. Although the nodal masses slightly change during the process, the results obtained by this approach are practically identical with those previously obtained.

The problem was also computed by using a plane approach. We used the approach given by

$$\begin{aligned} \mathbf{b}_r &= \bar{r} \mathbf{b}_x, & V &= \bar{r} A, \\ \mathbf{b}_z &= \bar{r} \mathbf{b}_y, & M_{IJ} &= \frac{1}{4} \delta_{IJ} \rho V, \\ \mathbf{c} &= \frac{1}{4} A \mathbf{s}, & \boldsymbol{\gamma} &= \mathbf{h} \end{aligned} \quad (37a)$$

where

$$\bar{r} = \frac{1}{4} (r_1 + r_2 + r_3 + r_4) \quad (37b)$$

is the average element radius.

The vectors $\mathbf{b}_x, \mathbf{b}_y$ are components of the \mathbf{B} matrix for plane Cartesian geometry and are given in [1, 2].

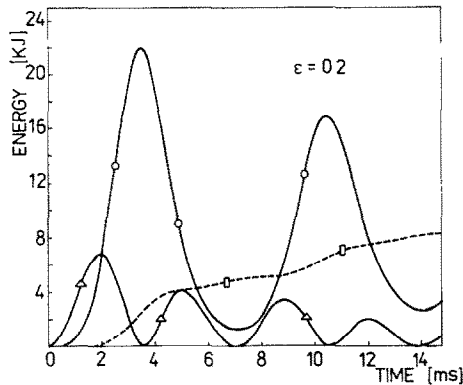


Fig. 15. Energy time histories for viscous HG control.
 ○: deformation energy; △: kinetic energy;
 □: dissipated HG energy.

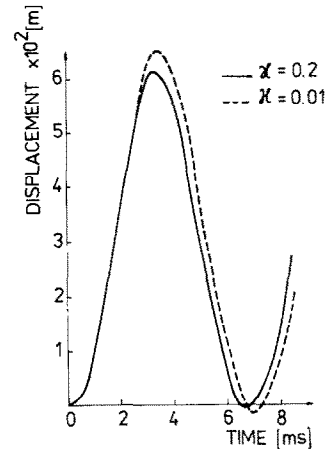


Fig. 16. Displacement of point A for various values of parameter κ . Plane approach.

The results obtained are presented in Figs. 16 and 17. The approach gives quite reasonable results in displacements, at least for the problem analyzed, and also well stabilizes the mesh already for small values of κ . However, the following points about plane approach given by (37), are noteworthy:

- Generally, the gradients of linear field are not evaluated correctly, that means, the consistency conditions are satisfied only approximately.
- The volume is evaluated correctly only for rectangular elements.
- The vector \mathbf{h} indicates the HG modes only approximately, that means, the corresponding HG control does not meet patch test.

The difference between plane and cylindrical approaches is significant only near the axis of symmetry. To compare the convergence rates of these two methods, the following example was chosen.

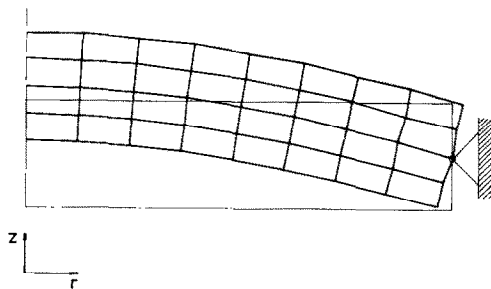


Fig. 17. Mesh deformation at time 3.81 ms for $\kappa = 0.01$. Plane approach.

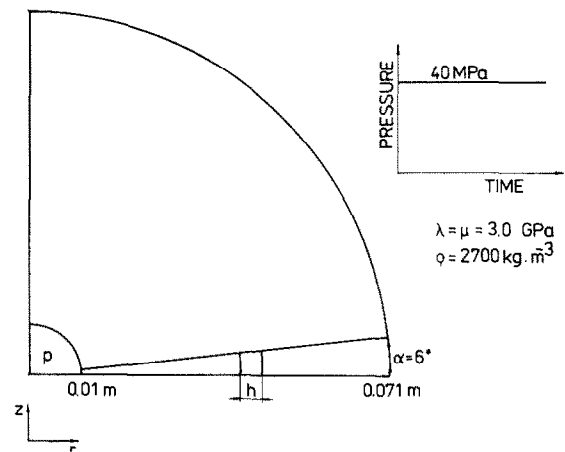


Fig. 18. Example 5.2. Wave propagation in spherical domain. Problem definition.

EXAMPLE 5.2. The domain with a central cavity is spherical. Hooke's law is considered. At time $t = 0$, the uniform pressure as the time step function is applied on the inside surface of the cavity. The problem definition is given in Fig. 18. The exact solution can be found in [9].

Although this is a one-dimensional wave propagation problem, a two-dimensional mesh with fourfold symmetry was used.

The discretization in circumferential direction was always the same. As regards the discretization in radial (spherical) direction, the thickness h of the elements, varied as follows: 0.001, 0.002, 0.004, and 0.008 m.

Linear ($a_l = 0.1$) and quadratic ($a_q = 4.0$) viscosities were used to prevent numerical oscillations due to shock wave and elastic HG control ($\kappa = 0.01$) to eliminate HG deformations. The result obtained for the cylindrical approach in radial (cylindrical) direction is illustrated in Fig. 19. The difference between the solutions in axial and radial direction was less than 1.5 percent.

To compare the displacement convergence rates, the following displacement norm was used:

$$(\text{displacement norm})^2 = \frac{1}{T} \int_0^T \frac{1}{V} \int_V (\mathbf{u}^{\text{exact}} - \mathbf{u}^{\text{FEM}})^t (\mathbf{u}^{\text{exact}} - \mathbf{u}^{\text{FEM}}) dV dt,$$

where the total time T of the computation was chosen so that the front of the wave arrived nearly to the outside surface of the domain. The results obtained are shown in Fig. 20. The cylindrical approach is more accurate, although the convergence rate seems to be the same. All calculations were performed using single precision (≈ 7 significant digits) on the EC 1034 machine. In Fig. 20, both approaches exhibit decreasing rate of convergence with mesh

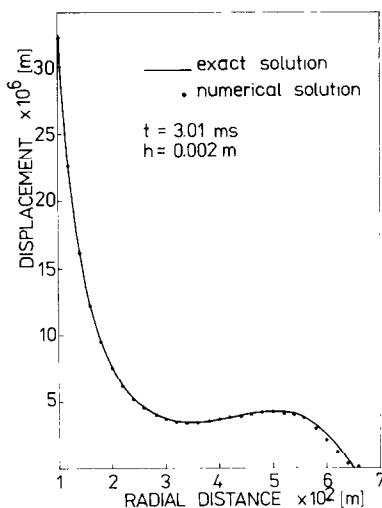


Fig. 19. Solution for the cylindrical approach in radial (r) direction.

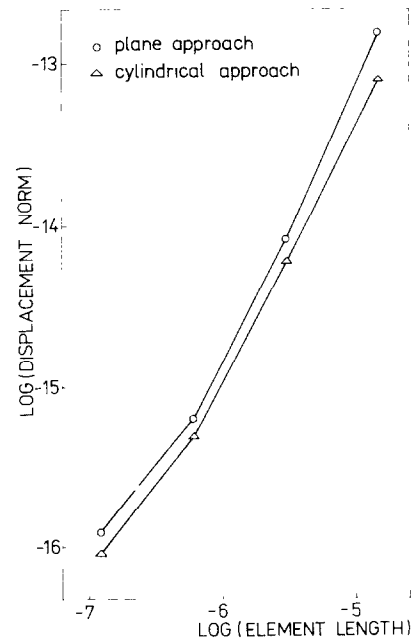


Fig. 20. Displacement convergence rates for both approaches.

refinement beyond a certain point; this behaviour is probably due to the use of single precision.

6. Conclusions

The one-point integration scheme for a general isoparametric quadrilateral in axisymmetric geometry and the procedure for controlling its HG modes have been developed by an algebraic approach. Simple examples assuming linear Hooke's law illustrate the effectiveness of this approach. The important aspects of the development are:

- The volume and uniform strain modes are integrated accurately, that means, the consistency conditions are satisfied.
- The cylindrical HG modes differ from plane Cartesian HG modes and must be computed for each element at each time step.
- The developed HG control satisfies the patch test whereas several alternatives do not.
- The elements near the axis of symmetry are stiffer than the ones far from the axis.

Even if the results presented here, and based on the plane approach, are quite reasonable, we can note:

- This approach, generally, does not satisfy consistency conditions and the corresponding HG control does not meet patch test and thus may deleteriously affect convergence [1].
- Although the displacement convergence rate seems to be the same, the cylindrical approach gives more accurate results
- The plane approach results in considerable cost saving, for our calculation the cylindrical approach increases computations by 40 percent.

Further analysis in this field is needed, especially for fluid dynamics where more severe mesh distortions can occur. Generally, we feel that the main benefits of the analytical integration scheme can be expected for Lagrangian or ALE(QE) codes in the field of fluid dynamics.

As regards solid mechanics, it is now possible to develop quadrilaterals with high coarse-mesh accuracy in cylindrical geometry adopting the development given in [7] for plane Cartesian geometry.

Appendix A

In this appendix, the explicit expressions for the vectors \mathbf{b}_r , \mathbf{b}_z , and \mathbf{c} given by (12) are presented.

The derivatives of any function $F(\xi, \eta)$ dependent on local coordinates are

$$\frac{\partial F}{\partial r} = \frac{1}{J} \left(\frac{\partial F}{\partial \xi} \frac{\partial z}{\partial \eta} - \frac{\partial F}{\partial \eta} \frac{\partial z}{\partial \xi} \right), \quad \frac{\partial F}{\partial z} = \frac{1}{J} \left(\frac{\partial F}{\partial \eta} \frac{\partial r}{\partial \xi} - \frac{\partial F}{\partial \xi} \frac{\partial r}{\partial \eta} \right), \quad (38a)$$

where

$$J = \frac{\partial r}{\partial \xi} \frac{\partial z}{\partial \eta} - \frac{\partial r}{\partial \eta} \frac{\partial z}{\partial \xi} \quad (38b)$$

is the Jacobian of the transformation between global r - z and local ξ - η coordinate systems. It holds:

$$s^t \Phi = 1. \quad (39)$$

Using (37), (38), (39), and (4) we can express the integrals in (12) in the form

$$b_{rI} = F_{KIJ} r_K z_J, \quad b_{zI} = F_{KJI} r_K r_J, \quad c_I = F_{IKJ} r_K z_J, \quad (40)$$

where

$$F_{IJK} = \int_{-1/2}^{1/2} \int_{-1/2}^{1/2} \Phi_I \left(\frac{\partial \phi_J}{\partial \xi} \frac{\partial \phi_K}{\partial \eta} - \frac{\partial \phi_J}{\partial \eta} \frac{\partial \phi_K}{\partial \xi} \right) d\xi d\eta. \quad (41)$$

The application of (12), (4), (39) and the use of relation $x_{i,j} = \delta_{ij}$ yields

$$b_i^t x_j = V \delta_{ij}, \quad c^t r = V, \quad c^t s = A. \quad (42)$$

For the element volume we get

$$V = F_{IJK} r_I r_J z_K. \quad (43)$$

From (40), (42), (43), it results that all “geometrical” variables can be calculated by means of nodal values x_{iI} and F_{IJK} coefficients, which are constant for any quadrilateral element.

Evaluation of F_{IJK} coefficients from (41) involves the integration of a polynomial which is at most biquadratic. Since the integration area is symmetric, only the constant and quadratic terms do not vanish. Therefore, we obtain

$$F_{IJK} = \frac{1}{16} s_I (A_{1J} A_{2K} - A_{2J} A_{1K}) + \frac{1}{48} [A_{1I} (A_{1J} h_K - A_{1K} h_J) + A_{2I} (A_{2K} h_J - A_{2J} h_K)]. \quad (44)$$

The matrix F_{IJK} is antisymmetric with respect to the second and third subscripts:

$$F_{IJK} = -F_{IKJ}, \quad F_{IJJ} = 0 \quad (\text{no sum on } J). \quad (45)$$

The conditions (45) reduce the number of evaluations to 24. However, the element volume has to be independent of the selection of node 1, which implies that F_{IJK} is invariant if the nodes are permuted according to the permutation Π_i , $i = 1, 2, 3$ defined in Table 1:

$$F_{IJK} = F_{\Pi_i(I)\Pi_i(J)\Pi_i(K)}, \quad i = 1, 2, 3. \quad (46)$$

The relations (46) confirm that only 6 terms of F_{IJK} need be evaluated. These terms may be evaluated via eq. (44) and (7). Six independent terms of F_{IJK} are listed in Table 2.

For practical computations, and especially for theoretical considerations, the following expressions derived from (40) and (44) are useful:

Table 1
Nodal permutation

	1	2	3	4
Π_1	4	1	2	3
Π_2	3	4	1	2
Π_3	2	3	4	1

Table 2
Six independent terms of F_{IJK}

I	J	K	F_{IJK}
1	1	2	$\frac{2}{12}$
1	1	3	0
1	1	4	$-\frac{2}{12}$
1	2	3	$\frac{1}{12}$
1	2	4	$\frac{1}{12}$
1	3	4	$\frac{1}{12}$

$$\begin{aligned}
b_1 &= \frac{1}{16}[(s^t r)(\Lambda_2^t z) + \frac{1}{3}(\Lambda_1^t r)(h^t z)]\Lambda_1 - \frac{1}{16}[(s^t r)(\Lambda_1^t z) + \frac{1}{3}(\Lambda_2^t r)(h^t z)]\Lambda_2 \\
&\quad + \frac{1}{48}[-(\Lambda_1^t r)(\Lambda_1^t z) + (\Lambda_2^t r)(\Lambda_2^t z)]h, \\
b_2 &= -\frac{1}{16}[(s^t r)(\Lambda_2^t r) + \frac{1}{3}(\Lambda_1^t r)(h^t r)]\Lambda_1 + \frac{1}{16}[s^t r)(\Lambda_1^t r) + \frac{1}{3}(\Lambda_2^t r)(h^t r)]\Lambda_2 \\
&\quad + \frac{1}{48}[(\Lambda_1^t r)^2 - (\Lambda_2^t r)^2]h, \\
c &= \frac{1}{4}As + \frac{1}{48}[(\Lambda_1^t r)(h^t z) - (\Lambda_1^t z)(h^t r)]\Lambda_1 + \frac{1}{48}[(\Lambda_2^t z)(h^t r) - (\Lambda_2^t r)(h^t z)]\Lambda_2.
\end{aligned} \tag{47}$$

From the above expressions we get

$$b_i^t s = 0, \quad c^t h = 0. \tag{48}$$

Finally, the explicit counterparts of (47) are, for example,

$$\begin{aligned}
b_{r_1} &= \frac{1}{12}[(2r_1 + r_3)(z_2 - z_4) + r_2(2z_2 - z_3 - z_4) + r_4(z_2 + z_3 - 2z_4)], \\
b_{z_2} &= \frac{1}{6}(r_1 + r_2 + r_3)(r_1 - r_3), \\
c_1 &= \frac{1}{12}[(2r_1 - r_3)(z_2 - z_4) + r_2(z_3 + z_4 - 2z_1) + r_4(2z_1 - z_2 - z_3)].
\end{aligned} \tag{49}$$

Appendix B

A frequency analysis of a cylindrical quadrilateral with one-point integration and a lumped mass matrix is useful because it provides a bound on eigenvalues needed for both the generalized HG stresses and the time criterion of explicit algorithms. To evaluate eigenvalues of the element, we follow the paper [3].

The natural modes and frequencies will be obtained from the following two equations:

$$Kv = \omega^2 Mv, \tag{50}$$

$$Kv = f^{\text{int}}. \tag{51}$$

The general isotropic hypoelastic stress-strain relation is

$$\boldsymbol{\sigma} = \mathbf{C} \boldsymbol{\varepsilon} , \quad (52)$$

where \mathbf{C} is given by (32).

For a cylindrical quadrilateral the mass and stiffness matrix are

$$\mathbf{M} = \frac{1}{4} \rho V \mathbf{I} , \quad (53)$$

$$\mathbf{K} = \frac{1}{V} \mathbf{B}^t \mathbf{C} \mathbf{B} , \quad (54)$$

where \mathbf{I} is unit 8×8 matrix, \mathbf{B} is defined by (16), and V is the element volume.

Note that for the mass matrix we use the “ $\frac{1}{4}$ approach”. This form of the matrix enables to find a bound on eigenvalues quite easy.

The counterpart of (54) is

$$\mathbf{K} = \frac{1}{V} \left[\begin{array}{c|c} (\lambda + 2\mu)[\mathbf{b}_r \mathbf{b}_r^t + \mathbf{c} \mathbf{c}^t] + \lambda[\mathbf{b}_r \mathbf{c}^t + \mathbf{c} \mathbf{b}_r^t] + \mu[\mathbf{b}_z \mathbf{b}_z^t] & \lambda[(\mathbf{b}_r + \mathbf{c}) \mathbf{b}_z^t] + \mu[\mathbf{b}_z \mathbf{b}_r^t] \\ \hline \lambda[\mathbf{b}_z (\mathbf{b}_r + \mathbf{c})^t] + \mu \mathbf{b}_r \mathbf{b}_z^t & (\lambda + 2\mu)[\mathbf{b}_z \mathbf{b}_z^t] + \mu[\mathbf{b}_r \mathbf{b}_r^t] \end{array} \right] . \quad (55)$$

The nodal force vector is given by

$$\mathbf{f}^{\text{int}} = \left\{ \begin{array}{c} \sigma_{rr} \mathbf{b}_r + \sigma_{rz} \mathbf{b}_z + \sigma_{\varphi\varphi} \mathbf{c} \\ \sigma_{rz} \mathbf{b}_r + \sigma_{zz} \mathbf{b}_z \end{array} \right\} . \quad (56)$$

Letting

$$\nu = \frac{\rho V}{4} \omega^2 , \quad (57)$$

and combining (50) and (51), we obtain

$$\nu \mathbf{I} \mathbf{v} = \mathbf{f}^{\text{int}} . \quad (58)$$

Using (56) and (58) we can see that the vector \mathbf{v} has to have the following form:

$$\mathbf{v} = \left\{ \begin{array}{c} \sigma_{rr} \mathbf{b}_r + \sigma_{rz} \mathbf{b}_z + \sigma_{\varphi\varphi} \mathbf{c} \\ \sigma_{rz} \mathbf{b}_r + \sigma_{zz} \mathbf{b}_z \end{array} \right\} . \quad (59)$$

Note that vectors \mathbf{b}_i and \mathbf{c} are linearly independent.

We define a 2×2 matrix \mathbf{a} by

$$a_{ij} = \mathbf{b}_i^t \mathbf{b}_j . \quad (60)$$

We denote the matrix \mathbf{a} in its principal orientation as $\hat{\mathbf{a}}$. In this case $\hat{\mathbf{a}}$ is a diagonal matrix:

$$\hat{\mathbf{a}} = \begin{bmatrix} \hat{a}_{11} & 0 \\ 0 & \hat{a}_{22} \end{bmatrix}, \quad (61)$$

where \hat{a}_{ii} are the eigenvalues of \mathbf{a} and the following relation holds:

$$a_{11} + a_{22} = \hat{a}_{11} + \hat{a}_{22} = \mathbf{b}_i^t \mathbf{b}_i. \quad (62)$$

Evaluating $\mathbf{K}\mathbf{v}$ in terms of \mathbf{b}_i and \mathbf{c} from (55), (59), defining the terms

$$\mathbf{e}_i = \mathbf{c}^t \mathbf{b}_i, \quad (63)$$

and using (60), we can compare the result obtained with the right-hand side of (50).

By this procedure five homogeneous equations are obtained. After the elimination of one dependent row (note that \mathbf{b}_i and \mathbf{c} are linearly independent) from these equations we have

$$\begin{bmatrix} (\lambda + 2\mu)a_{rr} + \lambda e_r - \nu' & \lambda a_{zz} & (\lambda + 2\mu)e_r + \lambda \mathbf{c}^t \mathbf{c} & 2(\lambda + \mu)a_{rz} + \lambda e_z \\ \lambda(a_{rr} + e_r) & (\lambda + 2\mu)a_{zz} - \nu' & \lambda(e_r + \mathbf{c}^t \mathbf{c}) & 2(\lambda + \mu)a_{rz} + \lambda e_z \\ \lambda(a_{rr} + e_r) + 2\mu e_r & \lambda a_{zz} & (\lambda + 2\mu)\mathbf{c}^t \mathbf{c} + \lambda e_r - \nu' & (\lambda + 2\mu)e_z + 2\lambda a_{rz} \\ \mu a_{rz} & \mu a_{rz} & \mu e_z & \mu(a_{rr} + a_{zz}) - \nu' \end{bmatrix} \begin{bmatrix} \sigma_{rr} \\ \sigma_{zz} \\ \sigma_{\varphi\varphi} \\ \sigma_{rz} \end{bmatrix} = \mathbf{0}, \quad (64)$$

where

$$\nu' = V\nu. \quad (65)$$

It is advantageous to express (64) in the principal direction of \mathbf{a} . Neglecting the terms \mathbf{e}_i and using

$$\hat{\mathbf{c}}^t \hat{\mathbf{c}} = \mathbf{c}^t \mathbf{c}, \quad (66)$$

we obtain the following eigenvalue equation:

$$\det \begin{bmatrix} (\lambda + 2\mu)\hat{a}_{rr} - \nu' & \lambda \hat{a}_{zz} & \lambda \mathbf{c}^t \mathbf{c} & 0 \\ \lambda \hat{a}_{rr} & (\lambda + 2\mu)\hat{a}_{zz} - \nu' & \lambda \mathbf{c}^t \mathbf{c} & 0 \\ \lambda \hat{a}_{rr} & \lambda \hat{a}_{zz} & (\lambda + 2\mu)\mathbf{c}^t \mathbf{c} - \nu' & 0 \\ 0 & 0 & 0 & \mu(\hat{a}_{rr} + \hat{a}_{zz}) - \nu' \end{bmatrix} = 0. \quad (67)$$

We directly obtain one eigenvalue:

$$\nu_4 = \frac{1}{V} \mu(\hat{a}_{rr} + \hat{a}_{zz}). \quad (68)$$

For other eigenvalues it is more useful to find a reasonable bound rather than solving a cubic equation.

A diagonal bound approach is used like in [3]:

$$\frac{1}{3}I_1 \leq \nu_{\max} \leq I_1, \quad (69)$$

where I_1 is the first invariant of the 3×3 matrix of (67). Using (62), it holds:

$$I_1 = \frac{1}{V} (\lambda + 2\mu)(\mathbf{b}_i^t \mathbf{b}_i + \mathbf{c}^t \mathbf{c}). \quad (70)$$

Maximum stiffness K_{\max} and frequency ω_{\max} , see (50), are therefore bounded by

$$\frac{1}{3V} (\lambda + 2\mu)(\mathbf{b}_i^t \mathbf{b}_i + \mathbf{c}^t \mathbf{c}) \leq K_{\max} \leq \frac{1}{V} (\lambda + 2\mu)(\mathbf{b}_i^t \mathbf{b}_i + \mathbf{c}^t \mathbf{c}), \quad (71)$$

$$\sqrt[4]{\frac{\lambda + 2\mu}{\rho} \frac{\mathbf{b}_i^t \mathbf{b}_i + \mathbf{c}^t \mathbf{c}}{V^2}} \leq \omega_{\max} \leq 2 \sqrt{\frac{\lambda + 2\mu}{\rho} \frac{\mathbf{b}_i^t \mathbf{b}_i + \mathbf{c}^t \mathbf{c}}{V^2}}. \quad (72)$$

During the above development the terms e_i defined by (63) have been omitted. It is worth to mention that these terms are zero exactly only for a rectangular element and generally can be neglected only for a slightly deformed quadrilateral.

References

- [1] T. Belytschko, J.S. Ong, W.K. Liu and J.M. Kennedy, Hourglass control in linear and nonlinear problems, *Comput. Meths. Appl. Mech. Engrg.* 43 (1984) 251–276.
- [2] D.P. Flanagan and T. Belytschko, A uniform strain hexahedron and quadrilateral with orthogonal hourglass control, *Internat. J. Numer. Meths. Engrg.* 17 (1981) 679–706.
- [3] T. Belytschko and J.I. Lin, Eigenvalues and stable time steps for the bilinear Mindlin plate element, *Internat. J. Numer. Meths. Engrg.* 21 (1985) 1729–1745.
- [4] V. Adamík and P. Matejovič, FINEDAN—An explicit finite element code for two-dimensional continuum dynamic analyses, Rept. 98/86, Nuclear Power Plants Research Institute, Trnava, Czechoslovakia, 1986 (in Czech).
- [5] J.M. Kennedy and T.B. Belytschko, Theory and application of a finite element method for arbitrary Lagrangian–Eulerian fluids and structures, *Nuclear Engrg. Design* 68 (1981) 129–146.
- [6] A.K. Gupta and B. Mohraz, The three-dimensional isoparametric element in curvilinear coordinates, *Nuclear Engrg. Design* 22 (1972) 301–304.
- [7] T. Belytschko and W.E. Bachrach, Efficient implementation of quadrilaterals with high coarse-mesh accuracy, *Comput. Meths. Appl. Mech. Engrg.* 54 (1986) 279–301.
- [8] O.-P. Jacquotte and J.T. Oden, Analysis of hourglass instabilities and control in underintegrated finite element methods, *Comput. Meths. Appl. Mech. Engrg.* 44 (1984) 339–363.
- [9] H.F. Cooper, Jr., Generation of an elastic wave by quasi-static isentropic expansion of a gas in a spherical cavity; comparison between finite difference predictions and the exact solution, AFWL-TR-66-83, 1966.